Accuracy Analysis of Ionospheric Prediction Models for Repairing Cycle Slips for BeiDou Triple-Frequency Observations

Yao Yifei[1], Cao Xinyun[2,3,4], Chang Guobin[5] and Geng Hongsuo[1]

[1](*College of Water Resources and Architectural Engineering, Northwest A&F University, Yangling, China*)
[2](*Key Laboratory of Virtual Geographic Environment, Nanjing Normal University, Ministry of Education, Nanjing, China*)
[3](*Jiangsu Center for Collaborative Innovation in Geographical Information Resource Development and Application, Nanjing, China*)
[4](*School of Geography Science, Nanjing Normal University, Nanjing, China*)
[5](*School of Environmental Science and Spatial Informatics, China University of Mining and Technology, Xuzhou, China*)
(E-mail: xycao@whu.edu.cn)

Both the code–phase combination and the Geometry-Free (GF) phase combination are widely employed to detect and repair cycle slips for BeiDou Navigation Satellite System (BDS) triple-frequency observations. However, the effect of residual ionospheric delay on Narrow-Lane (NL) or GF observations must be considered to avoid incorrect cycle–slip estimation. To improve the accuracy in repairing cycle slips, a corrective ionospheric delay value predicted from the previous ionosphere sequence is used to amend the NL or GF observations at the current epoch. The main purpose of the work reported here is to evaluate the efficacy of a three-step method proposed to detect and repair cycle slip using two extra-wide-lane code–phase and one GF phase combination observations. BDS triple-frequency data were processed in two stages: separate processing of geosynchronous Earth orbit satellites, and the division of inclined geosynchronous satellite orbit and medium Earth orbit satellites into two groups for processing at 30° elevation thresholds. Results revealed that using the prediction models to correct NL or GF observations could ensure a rounding success rate of cycle slip close to 100%, even under high ionospheric activity.

1. INTRODUCTION.   Cycle slips are discontinuities in the carrier phase, represented as integer numbers of wavelengths, attributable to external interference and obstacles in the

path of satellite signals, which could cause temporary loss of lock. For precise positioning, any cycle slip related to ambiguity should be corrected, and the effectiveness of cycle–slip repair is reflected directly in data quality and precise positioning results (Li et al., 2016). Methods for the detection and repair of cycle slip can be divided into two categories: differential observations and un-differenced observations.

In the first strategy, double-difference observations can eliminate or greatly reduce most errors from both the satellite and the receiver. It should be noted that because the single-difference observation strategy has more parameters to be estimated, it is seldom employed. In case of the short baseline, the influences of ionospheric and tropospheric delays can be neglected. Thus, the cycle–slip value and other estimated parameters (for example, positional information) can all be solved based on the epoch-difference. However, the following problems are inherent in the double-difference strategy: (1) at least four common satellites are needed; (2) when the length of the baseline is long, the effect of atmospheric delay errors has to be considered; (3) the cycle–slip repair processing of the reference satellite is cumbersome; and (4) two epoch observations must be initialised without cycle slip. Compared with the un-differenced strategy, the double-difference strategy has huge advantages in repairing cycle slip for a single-frequency receiver with a short baseline.

One of the most widely used alternative methods in the second strategy is the improved TurboEdit algorithm (Blewitt, 1990), which is generally used together with the Melbourne–Wübbena combination in the detection of large cycle slips (Hatch, 1982; Melbourne, 1985; Wübbena, 1985). The TurboEdit and Melbourne–Wübbena combination is effective in detecting most cycle slips. For example, Liu et al. (2010) proposed an improved method to detect and repair cycle slip based on the Melbourne–Wübbena combination and the total electron content rate, assuming that the ionospheric delay remained stable over a short period (1·0 s in the literature). Cai et al. (2012) proposed a forward and backward moving window averaging method and a time differential ionospheric residual method, which could detect cycle slip, even under active ionospheric delay.

In future, Global Navigation Satellite Systems (GNSS) will adopt three or more carrier frequencies (Zhang and Li, 2015). Although Li et al. (2011) proposed a code–phase combination method, ionospheric influence on the accuracy of cycle slip was not considered under low elevation angles. Huang et al. (2015) proposed the use of the Geometry-Free (GF) phase combination to detect and repair cycle slip, and they promoted the use of the least-square ambiguity decorrelation adjustment algorithm to verify whether the cycle slip was repaired properly (Teunissen, 1995; Huang et al., 2015). Zhao et al. (2014) proposed a method using three code–phase combinations, after ionospheric correction, to detect and repair cycle slip for triple-frequency phase-carrier observations. Similarly, Yao et al. (2016) proposed the combined use of two code–phase combinations and one GF phase combination after simple ionospheric rectification. The above two methods are similar in principle. The former first corrects the Narrow-Lane (NL) code–phase combination using the previous ionospheric delay and then rounds the float cycle–slip estimation for the NL combination, while the cycle slips at the other two Extra-Wide-Lane (EWL) combinations are solved, whereas the latter first corrects the GF phase combination and then rounds the three float cycle–slip estimations. As the short wavelength of the NL combination and the GF combination are very susceptible to ionospheric delay, the residual ionospheric delay directly determines the efficiency and success rate of cycle–slip repair. However, neither study included a detailed analysis and comparison of ionospheric prediction methods, especially under active ionospheric conditions.

The remainder of this paper is organised as follows. First, Section 2.1 describes the three-step process method, which includes the EWL code–phase and GF phase cycle–slip detection and repair for triple-frequency observations and the ionospheric delay estimation method. Then, Section 2.2 analyses the four types of improved prediction model. In Section 3, we discuss the effects of epoch differential ionospheric delay variation based on satellite type and elevation angle, and we use real BeiDou Navigation Satellite System (BDS) data to evaluate the accuracy of the four improved prediction models, including ionospheric stability conditions and high ionosphere activity. Section 4 summarises the derived research conclusions and outlines future prospects.

2. THEORETICAL ANALYSIS.   First, we introduce the three-step process method used for cycle–slip detection and repair. Furthermore, the effect of ionospheric delay on the accuracy of combinational observations is assessed. Then, regarding the core issue, four representative models are introduced and analysed to improve the accuracy of the predicted ionospheric delay.

2.1.   *The three-step method to detect cycle slip.*   The first step of the proposed method involves linearly independent detection of the amount of cycle slip, which is achieved by combining two EWL code–phase and one GF phase combination. Then, the ionospheric delay variation is predicted using the preceding observation sequence without cycle slip, which is used to correct the GF combined observations. Finally, the EWL and the corrected GF combination are used to detect and repair the cycle slip.

Based on the theory of the triple-frequency combination, the combinational observations of phase and code can be described as follows (Richert and El-Sheimy, 2007; Cocard et al., 2008; Urquhart, 2009; Yao et al., 2016):

$$\lambda_{ijk}\varphi_{ijk} = \rho - \lambda_{ijk}N_{ijk} + T + \delta_{orb} - \eta_{ijk}I_1 + cdt_{ijk} + B_{ijk} + \lambda_{ijk}\varepsilon_{ijk} \tag{1}$$

$$R_{abc} = \rho + T + \delta_{orb} + \eta_{abc}I_1 + cdt_{abc} + b_{abc} + \varepsilon_{abc} \tag{2}$$

$$\eta_{ijk} = \lambda_{ijk}/\lambda_1(i + j\lambda_2/\lambda_1 + k\lambda_3/\lambda_1)$$

$$\eta_{abc} = a + b(\lambda_2/\lambda_1)^2 + c(\lambda_3/\lambda_1)^2$$

$$\varepsilon_{ijk} = i\varepsilon_1 + j\varepsilon_2 + k\varepsilon_3, \varepsilon_{abc} = ae_1 + be_1 + ce_3$$

where φ_{ijk} and R_{abc} are the combinational carrier phase (unit: cycles) and code (unit: m) observations, respectively, subscripts i, j and k are integers that are not all zero, and a, b and c are real numbers, where $a = b = c = 1/3$ adopted here is to minimise the impact of code noise. The combinational ambiguities $N_{ijk} = iN_1 + jN_2 + kN_3$ and N_1, N_2 and N_3 are the ambiguities of the three frequencies. The combinational wavelength $\lambda_{ijk} = \lambda_1\lambda_2\lambda_3/(i\lambda_2\lambda_3 + j\lambda_1\lambda_3 + k\lambda_1\lambda_2)$, where λ_1, λ_2 and λ_3 are the wavelengths of the three frequencies. Furthermore, T is the tropospheric delay, δ_{orb} represents satellite orbit errors, I_1 is the ionospheric delay of the B1 frequency, η_{ijk} and η_{abc} are ionospheric influence coefficients of the combinational phase and code, respectively, cdt_{ijk} and cdt_{abc} are clock errors of the combinational phase and code, respectively, B_{ijk} and b_{abc} are hardware delays of phase and code combinations, respectively, ε_{ijk} and ε_{abc} represent the noise of the phase and code combinations, respectively and ε and e represent the noise of the original frequency phase and code, respectively.

Based on the above equations, in adjacent epochs, the epoch difference $\Delta N_{ijk,abc}$ of the combinational code–phase observations can be formulated as:

$$\Delta N_{ijk,abc} = (\Delta R_{abc}/\lambda_{ijk} - \Delta\varphi_{ijk}) - \eta_{ijk,abc}\Delta I_1 - (\Delta\varepsilon_{abc}/\lambda_{ijk} - \Delta\varepsilon_{ijk}) \qquad (3)$$
$$\eta_{ijk,abc} = (\eta_{abc} + \eta_{ijk})/\lambda_{ijk}$$

where Δ denotes the single difference in the adjacent epochs and $\eta_{ijk,abc}$ is the ionospheric influence coefficient of the combinational code–phase observations. Most errors can be eliminated or greatly reduced by the single difference in adjacent epochs, such as orbit error, clock error, tropospheric delay and multipath errors. As seen in Equation (3), ρ, T and δ_{orb} can be eliminated, while other errors can be reduced considerably. In addition, the cycle–slip value is affected both by the ionosphere and by noise. When a code–phase combination with a larger wavelength is adopted, we can ignore the influence of noise on the cycle–slip value. Furthermore, the effect of ionospheric delay can be reduced by selecting a small influence coefficient, particularly for low-sampling-rate observations or highly active ionospheric conditions. Without consideration of the influence of ionospheric delay, the cycle–slip value can be rewritten as follows:

$$\Delta N_{ijk,abc} = (\Delta R_{abc}/\lambda_{ijk} - \Delta\varphi_{ijk}) - (\Delta\varepsilon_{abc}/\lambda_{ijk} - \Delta\varepsilon_{ijk}) \qquad (4)$$

From Equation (4), it is evident that because of the large noise of the code observations, the combinational wavelength has considerable impact on the Standard Deviation (STD) of the cycle–slip value. Therefore, the combinational wavelength is the most important parameter, followed in descending order by the combinational coefficient and the ionospheric influence coefficient. For details on the best code–phase combinations, the reader is referred to Richert and El-Sheimy (2007) and Urquhart (2009). Here, consistent with Yao et al. (2016), the optimal code–phase combinations of $(0, 1, -1)$ and $(1, -5, 4)$ are employed as the first and second detectable cycle–slip amounts.

Zhao et al. (2014) introduced an NL combination as a third detectable cycle–slip amount to ensure linear independence of the three employed amounts. In contrast from this strategy, Yao et al. (2016) introduced a GF phase combination to ensure mutual independence. Both methods correct the third detectable amount using the predicted ionospheric delay based on previous observations, which is because the ionospheric delay has the greatest impact on the NL code–phase combination or the GF phase combination. Moreover, both methods were used to solve the cycle–slip value ΔN_3 and for rounding purposes. Although the two methods employ the third different cycle–slip detectable amount, we believe the difference between the two methods is negligible.

Consistent with Yao et al. (2016), the following GF phase combination is adopted:

$$\begin{aligned}
L_{\alpha\beta\gamma} &= \alpha\lambda_1\varphi_1 + \beta\lambda_2\varphi_2 + \gamma\lambda_3\varphi_3 = -N_{\alpha\beta\gamma} - \eta_{\alpha\beta\gamma}I_1 + \varepsilon_{\alpha\beta\gamma} \\
N_{\alpha\beta\gamma} &= \alpha\lambda_1N_1 + \beta\lambda_2N_2 + \gamma\lambda_3N_3 \\
\eta_{\alpha\beta\gamma} &= \alpha\lambda_1 + \beta\lambda_2^2/\lambda_1 + \gamma\lambda_3^2/\lambda_1 \\
\varepsilon_{\alpha\beta\gamma} &= \alpha\lambda_1\varepsilon_1 + \beta\lambda_2\varepsilon_2 + \gamma\lambda_3\varepsilon_3
\end{aligned} \qquad (5)$$

where $L_{\alpha\beta\gamma}$ is the GF phase combinational observation (unit: m) and subscripts α, β and γ are the combinational coefficients. To eliminate the impact of geometrical distance, troposphere delay and satellite orbit error, let $\alpha + \beta + \gamma = 0$. Parameters $N_{\alpha\beta\gamma}$, $\eta_{\alpha\beta\gamma}$, $cdt_{\alpha\beta\gamma}$, and

$\varepsilon_{\alpha\beta\gamma}$ are the combinational ambiguity, ionospheric amplification factor (different from the ionospheric influence coefficient η_{abc}), clock errors and noise of the GF phase combinational observation, respectively. In adjacent epochs, the detectable cycle–slip value $\Delta N_{\alpha\beta\gamma}$ of the GF phase by epoch difference can be resolved as follows:

$$\Delta N_{\alpha\beta\gamma} = -\Delta L_{\alpha\beta\gamma} - \eta_{\alpha\beta\gamma}\Delta I_1 + \Delta\varepsilon_{\alpha\beta\gamma} \qquad (6)$$

It can be seen from Equation (6) that the accuracy of the GF detectable cycle–slip value is affected mainly by the deviation value of the combinational ionospheric delay and stochastic noise. Due to the smaller amount of noise associated with phase combinational observations, the most important factor is the ionospheric delay. Thus, because the ionospheric delay has the greatest influence on the GF observation, it has to be corrected by the prediction model when ionospheric delay is greater than the threshold value (for example, 41·9 mm). It is important to note that the combinational ionospheric delay variance $\eta_{\alpha\beta\gamma}\Delta I_1$ (replaced by ION in this paper, which is the slant ionospheric delay variance of the GF phase combination) predicted and corrected in this paper is not the ionospheric delay variance of the B1 frequency. Therefore, the combinational ionospheric delay can be minimised by selecting a small ionospheric amplification factor for the prediction and correction model. The prediction model of ionospheric delay variance can be expressed as follows:

$$\eta_{\alpha\beta\gamma}\Delta I_1^k = f\left(\eta_{\alpha\beta\gamma}\Delta I_1^{k-m}, \ldots, \eta_{\alpha\beta\gamma}\Delta I_1^{k-1}\right) \qquad (7)$$

where $f(\ldots)$ denotes the mapping function of the ionospheric delay. Here, superscript k denotes the current epoch location and superscript m denotes the number of epochs needed to reflect the ionospheric delay variance rates (the size of window). As previous epochs have no cycle slip, we can obtain the preceding ionospheric delay sequence for the prediction of the subsequent ionospheric delay. In contrast to Chang et al. (2018), to eliminate or greatly reduce the influence of the geometric part, geometric distance, tropospheric delay, satellite orbit, and satellite clock, and to improve the accuracy of the estimated ionospheric delay, the following equation is constructed to solve the preceding ionospheric delay sequence and to both predict the ionospheric delay variance and repair cycle slip in the next epoch:

$$\begin{bmatrix} \lambda_1\Delta\varphi_1 - \lambda_2\Delta\varphi_2 - \lambda_1\Delta N_1 + \lambda_2\Delta N_2 \\ \lambda_1\Delta\varphi_1 - \lambda_3\Delta\varphi_3 - \lambda_1\Delta N_1 + \lambda_3\Delta N_3 \end{bmatrix}$$
$$= \begin{bmatrix} -1 + \lambda_2^2/\lambda_1^2 \\ -1 + \lambda_3^2/\lambda_1^2 \end{bmatrix}\Delta I_1 + \begin{bmatrix} \Delta\xi_1 + \Delta\xi_2 \\ \Delta\xi_1 + \Delta\xi_3 \end{bmatrix} = A\Delta I_1 + \Delta\xi \qquad (8)$$

where ΔN_1, ΔN_2, and ΔN_3 are the cycle–slip values of the three frequencies and ΔI_1 is the ionospheric delay variance of the B1 frequency. In summary, two code–phase combinations and one GF combination are employed to solve the original cycle–slip value, and the resolving equation is constructed as follows:

$$BX = L \qquad (9)$$

$$B = \begin{bmatrix} i_1 & j_1 & k_1 \\ i_2 & j_2 & k_2 \\ \alpha\lambda_1 & \beta\lambda_2 & \gamma\lambda_3 \end{bmatrix}, \quad X = [\Delta N_1 \quad \Delta N_2 \quad \Delta N_3]^{\mathrm{T}}, \quad L = [n_1 \quad n_2 \quad n_3]^{\mathrm{T}}$$

$$n_1 = \text{round}(\Delta N_{(1,-1,0)}), \quad n_2 = \text{round}(\Delta N_{(1,-5,4)}), \quad n_3 = -\Delta L_{\alpha\beta\gamma}^k - \eta_{\alpha\beta\gamma}\Delta I_1^k$$

where round($\cdot$) denotes direct rounding. Because the STD of the selected code–phase combination is so small that the success rate of rounding is >99·99% (Yao et al., 2016), we can regard n_1 and n_2 as correct. Compared with the selected code–phase combination, the observational accuracy of the GF combination is weak because of the influence of the ionospheric delay. In short, the accuracy of an unknown cycle–slip value depends mainly on that of the modified ionospheric delay. Through calculation and analysis based on Equation (9), it can be concluded that: the ionospheric delay variance ΔI_1 of the B1 frequency must be <41·9 mm to ensure correct rounding of the cycle slip with the corresponding value of *ION* <28·2 mm (ignoring the impact of observed noise).

The cycle slip value X of the triple-frequency original carrier observations can be obtained using Equation (9). As the rounding success rate of the EWL combinations is >99·99%, we can ignore the impact of the EWL combinations on the estimated original carrier cycle slip. Therefore, the original carrier cycle–slip value is affected only by the residual errors of the GF combined observations, which is why we adopted the simplest form of integer rounding. If a higher success rate were desired, the integer least-squares method could be adopted (Teunissen, 2002).

The original phase observations generate cycle slip as follows:

$$n_1 \neq 0 \text{ or } n_2 \neq 0 \text{ or } \Delta N_3 \neq 0 \tag{10}$$

where n_1, n_2 and ΔN_3 are the three detectable cycle–slip amounts.

2.2.   *Prediction models for ionospheric delay.*   There are many prediction models for time series data. Considering the ionosphere delay associated with the variation of satellite elevation angle and the slow variation in sequential epochs, four representative prediction models are employed to test the accuracy of the ionospheric delay predictions: the Sliding Window Mean (SWM) method, Weighted SWM (WSWM) method, Polynomial Fitting (PF) method, and Kalman Filtering (KF) method.

First, when the satellite elevation angle varies slowly or there is a small sampling interval (for example, 1 s), the variation of ionospheric delay can be ignored. In such cases, the SWM model could represent an efficient method. However, for larger sampling intervals (for example, 30 s), the variation of ionospheric delay could be reasonably large, meaning the sliding window constitutes the optimal strategy. Second, because ionospheric delay varies rapidly with time, introducing the WSWM method could provide fuller consideration of the trend by adding a weighted factor for the predicted epoch according to the interval between the sampling point and the predicted point. Third, when the ionospheric delay varies linearly or nonlinearly, the PF method can simulate the variational process based on the least squares method. The PF method is the one used most commonly. For example, the parabolic method, Lagrangian fitting and exponential smoothing are all approximations of the PF method. The PF method can replace other methods when applied to a local area. In addition, the widely used total electron content rate method (Liu, 2010) can be considered as an example of the PF method that uses just three sampling points. Finally, the KF method can be used as a representative fitting method to predict ionospheric delay with consideration of process noise.

2.2.1.   *Sliding Window Mean (SWM) method.*   Because of the real-time processing required to detect and repair cycle slip, we selected several previous epochs without cycle

slip to estimate *ION*, rather than use a similar forward and backward moving window averaging method. Given that no cycle slip existed before this epoch, we can accurately reflect the ionospheric delay variance rates and trends as follows:

$$\eta_{\alpha\beta\gamma}\Delta I_1^k = f\left(\eta_{\alpha\beta\gamma}\Delta I_1^{k-m}, \ldots, \eta_{\alpha\beta\gamma}\Delta I_1^{k-1}\right) = \frac{1}{m}\sum_{i=1}^{m}\eta_{\alpha\beta\gamma}\Delta I_1^{k-i} \tag{11}$$

It should be noted that the size of the sliding window (called *m*) has a certain impact on the accuracy and therefore it cannot be too large or too small; here, we adopted a value of about 20.

2.2.2. *Weighted Sliding Window Mean (WSWM) method.* As ionospheric delay varies rapidly with time, introducing a weighted method can include consideration of the trend of ionosphere delay more fully by adding a weighted factor for the predicted epoch according to the interval between the sampling point and the predicted point.

In considering the trend of change of ionospheric delay for Inclined Geosynchronous Satellite Orbit (IGSO) and Medium Earth Orbit (MEO) satellites, a weighting factor is employed to construct the WSWM as follows:

$$\eta_{\alpha\beta\gamma}\Delta I_1^k = f\left(\eta_{\alpha\beta\gamma}\Delta I_1^{k-m}, \ldots, \eta_{\alpha\beta\gamma}\Delta I_1^{k-1}\right) = \frac{2}{m+1}\sum_{i=m}^{1}\frac{i}{m}\left(\eta_{\alpha\beta\gamma}\Delta I_1^{k-(m-i+1)}\right) \tag{12}$$

2.2.3. *Polynomial Fitting (PF) method.* Existing studies have shown that slant ionospheric delays of IGSO and MEO satellites are mostly parabolic in form with a decrease of satellite elevation angle. Furthermore, a parabolic model can adequately capture the temporal variation of ionospheric delay. The *k*-th epoch ionospheric delay can be expressed as the following equation:

$$\kappa(t)_k = \theta_0 + \theta_1 t_k + \theta_2 t_k^2 \tag{13}$$

where κ denotes the *k*-th epoch slant ionospheric delay *ION*, θ is the parabolic coefficient, and *t* is the time interval. Only the second-order PF need be employed because its accuracy is adequate. The ionospheric delay of *m* epochs can be expressed as:

$$\kappa = \tau\vartheta \tag{14}$$

where $\kappa = \begin{bmatrix} \kappa_1 \\ \vdots \\ \kappa_m \end{bmatrix}$, $\tau = \begin{bmatrix} 1 & t_1 & t_1^2 \\ \vdots & \vdots & \vdots \\ 1 & t_m & t_m^2 \end{bmatrix}$, and $\vartheta = \begin{bmatrix} \theta_0 \\ \theta_1 \\ \theta_2 \end{bmatrix}$. The estimated parameter ϑ can be calculated based on the previous *m* epochs using the following equation:

$$\vartheta = (\tau^{\mathrm{T}}\tau)^{-1}\tau^{\mathrm{T}}\kappa \tag{15}$$

2.2.4. *Kalman Fitting (KF) method.* To ensure the accuracy of the dynamic model, the time difference ionospheric delay, and its velocity and accelerated velocity are employed to construct the KF method (Chang et al., 2018). The prediction process is shown as follows:

$$\bar{x}_k = F\hat{x}_{k-1} \tag{16}$$

$$\bar{P}_k = F\hat{P}_{k-1}F^T + Q_{k-1} \tag{17}$$

where $F = \begin{bmatrix} 1 & t & \frac{t^2}{2} \\ 0 & 1 & t \\ 0 & 0 & 1 \end{bmatrix}$, $x = \begin{bmatrix} \kappa \\ \dot{\kappa} \\ \ddot{\kappa} \end{bmatrix}$, and $Q_{k-1} = \sigma_{\Delta\dddot{\kappa}}^2 \begin{bmatrix} \frac{t^5}{20} & \frac{t^4}{8} & \frac{t^3}{6} \\ \frac{t^4}{8} & \frac{t^3}{3} & \frac{t^2}{2} \\ \frac{t^3}{6} & \frac{t^2}{2} & t \end{bmatrix}$. Here, x is the estimated param-

eter, and κ, $\dot{\kappa}$, and $\ddot{\kappa}$ are the value, velocity, and accelerated velocity of the epoch difference ionospheric delay, respectively. The overbar denotes the predicted parameter, $\hat{x}$ denotes the estimated parameter, P is the covariance matrix, and Q denotes the observed noise.

The update process is shown as follows:

$$\hat{x}_k = (A^{\mathrm{T}}\tilde{Q}_k^{-1}A)^{-1}A^{\mathrm{T}}\tilde{Q}_k^{-1}y_k \tag{18}$$

$$\hat{P}_k = (A^{\mathrm{T}}\tilde{Q}_k^{-1}A)^{-1} \tag{19}$$

where $y_k = \begin{bmatrix} \bar{x}_k \\ \kappa_k \end{bmatrix}$ and $A = \begin{bmatrix} 1 & 0 & 0 \\ 0 & 1 & 0 \\ 0 & 0 & 1 \\ 1 & 0 & 0 \end{bmatrix}$. In contrast to Chang et al. (2018), ignoring the effects of

relevance, $\tilde{Q}_k = \begin{bmatrix} \bar{P} & 0 \\ 0 & \sigma_\kappa^2 \end{bmatrix}$. It should be noted that this combines the prediction by treating it as a virtual observation, and the ionospheric delay of the current epoch is used to construct the new observations.

To minimise the effect of the current epoch on the observed noise, and to reflect the continuity and trend of the variation of ionospheric delay, a memory factor is introduced as follows:

$$\sigma_{\ddot{\kappa}}^2 = (1 - \mu)\sigma_{\ddot{\kappa}}^2 + \mu\hat{\sigma}_{\ddot{\kappa}}^2 \tag{20}$$

where μ is the memory factor used to balance the current and previous epoch ionospheric delays.

3. EXPERIMENTAL ANALYSIS. Consistent with Chang et al. (2018), the actual triple-frequency observations used to evaluate the accuracy of the four prediction models were collected at station SHA1 on 13 November 2015 08:00–16:00 local time using the International GNSS Monitoring and Assessment System. This station is located in Shanghai, China (31·10°N, 121·20°E). The ionospheric delay on this day was reasonably stable and the corresponding Kp index, which indicates the severity of global magnetic disturbances in near-Earth space, was 1–4. The sampling interval was 30 s and the period of observation was approximately 8 h. The code–phase combination of coefficients $(0, 1, -1)$ and $(1, -5, 4)$ and the GF combination of coefficients $(1, 0, -1)$ were employed in cycle–slip detection and repair. Three types of satellite orbit (that is, Geosynchronous Earth Orbit (GEO), IGSO and MEO satellites) were used to analyse the statistical accuracy of the ionospheric delay and the rounding error of cycle slip.

3.1. *Correlation of ionospheric delay and satellite elevation angle.* Due to the different operating speeds of the various BDS orbital satellites, three types of satellite data were analysed independently to assess the statistical accuracy of the ionospheric delay and the rounding error of cycle slip. In addition, because the slant ionospheric delay is sensitive to satellite elevation angle, we segmented the time series data based on elevation angle thresholds.

Figure 1 shows the time series of the epoch difference ionospheric delay and elevation angle. It is evident that the ionospheric delay variation of satellite C01 is stable because
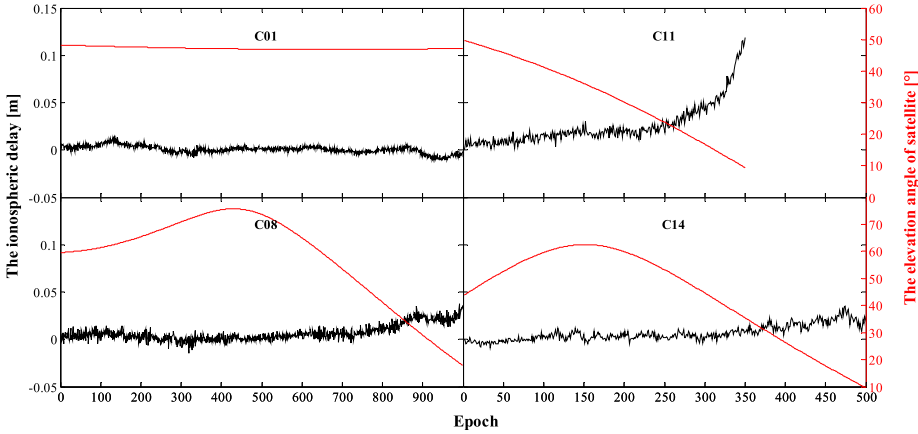
Figure 1.   Epoch difference ionospheric delay and elevation angle.

the elevation angle of GEO satellites remain largely unchanged. However, the ionospheric variation of satellite C11 can be sufficiently large that its effect on the accuracy of the GF combination must be considered. In particular, the ionospheric variation could reach the decimetre level when the elevation angle is <30°. The prediction accuracy of the ionospheric correction directly determines the success rate of rounding cycle slip. In addition, the noise of slant observations will begin to increase sharply (Gerdan, 1995). Therefore, four types of prediction model were employed and the threshold of the segmentation process was set at 30°.

3.2. *Statistical accuracy of EWL combination observations.*   The traditional experiment is to add a certain cycle–slip value to the original data in different epochs and then to use the employed model to detect and repair the cycle slip. However, this strategy is too inefficient and it cannot be used for evaluation in each epoch. More importantly, we found the accuracy of cycle–slip repair depended only on the observed data noise and the employed model. In the analysis, the following three statistics are used: mean (reflecting the effectiveness after ionospheric delay correction), maximum (reflecting whether the cycle–slip estimation is correct), and STD (reflecting the overall accuracy of cycle–slip repair).

The rounding errors of EWL combination float estimations, including the mean, maximum, and STD, are shown in Table 1. It is apparent that the rounding error STD of EWL_1 and EWL_2 for GEO satellites is 0·028 and 0·054 cycles, respectively. Such minor rounding errors have negligible impact on the cycle–slip estimation. In contrast to the GEO satellites, the corresponding STD for IGSO and MEO satellites is 0·07 and 0·09 cycles, respectively. The reason is that the ionospheric delay of GEO satellites is small, while that of IGSO and MEO satellites can be large, even up to the decimetre level, which affects the rounding accuracy of EWL combinations. Fortunately, the overall STD is still so small that the success rate remains >99·999997% (Li et al., 2014). It should be noted that because of the large wavelength of the EWL combinations, we have not corrected the EWL observations using the previous ionospheric delay. To improve the EWL rounding accuracy further, we should bring Equation (8) into Equation (3) to correct the estimated cycle–slip value using the calculated ionospheric values.

Table 1.   Rounding error of EWL float estimations (unit: cycles).

| PRN	Mean		Maximum		STD	
	EWL_1	EWL_2	EWL_1	EWL_2	EWL_1	EWL_2
C01	0·000	0·000	0·063	0·106	0·019	0·035
C02	0·000	−0·001	0·105	0·236	0·031	0·063
C03	0·000	0·000	0·082	0·189	0·024	0·049
C04	0·000	0·000	0·095	0·175	0·027	0·041
C05	0·000	−0·002	0·149	0·261	0·042	0·083
Average					0·028	0·054
C06	0·000	0·001	0·219	0·204	0·060	0·057
C07	0·001	−0·015	0·320	0·264	0·081	0·083
C08	0·000	−0·003	0·223	0·200	0·060	0·057
C09	0·000	0·002	0·237	0·225	0·069	0·066
C10	0·001	−0·009	0·304	0·401	0·086	0·100
Average					0·071	0·073
C11	0·002	−0·013	0·470	0·294	0·103	0·094
C14	0·000	−0·003	0·245	0·291	0·077	0·067
Average					0·090	0·081
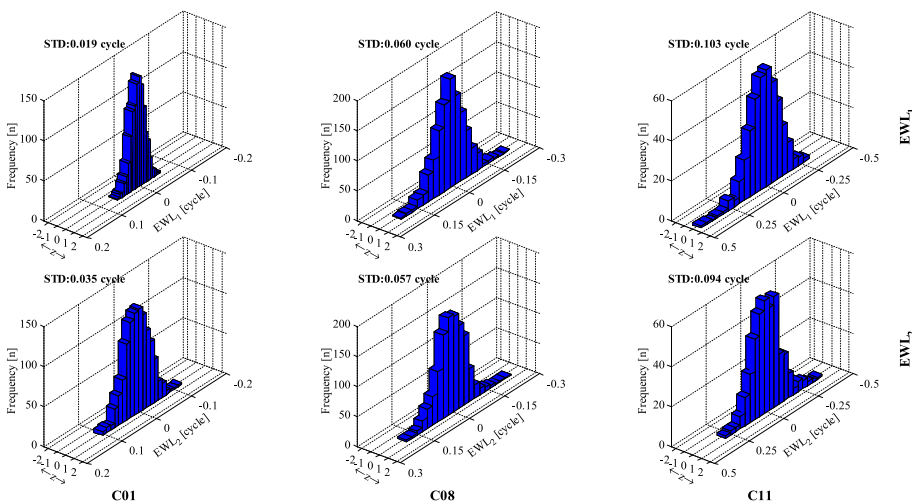
Figure 2.   Histograms of EWL rounding error: (top left) C01 EWL_1, (bottom left) C01 EWL_2, (top middle) C08 EWL_1, (bottom middle) C08 EWL_2, (top right) C11 EWL_1, and (bottom right) C11 EWL_2.

The statistical results are displayed as histograms in Figure 2 for the three selected satellites, that is, C01, C08 and C11. The rounding errors of the cycle–slip estimators follow Teunissen's distribution (Teunissen, 2002). It is evident that the STD increases gradually in the order of GEO to IGSO and then to MEO satellites; however, the success rate remains close to 100%.

3.3.   *Comparison of prediction model accuracy for GEO satellites.*   In contrast to EWL combinations, NL combinations have a smaller wavelength and therefore the effect of ionospheric delay on the observation must be taken into account. Four improved prediction models were used to predict the ionospheric delay and the rounding accuracy (fractional

Table 2.   Rounding accuracy of ΔN_3 for GEO satellites (unit: cycles).

PRN	Mean				Maximum				STD			
	SWM	WSWM	PF	KF	SWM	WSWM	PF	KF	SWM	WSWM	PF	KF
C01	0·000	0·000	0·000	0·000	0·126	0·133	0·135	0·136	0·033	0·035	0·036	0·035
C02	0·000	0·000	0·000	−0·001	0·153	0·160	0·193	0·175	0·045	0·047	0·052	0·054
C03	0·001	0·001	0·000	0·001	0·137	0·136	0·153	0·136	0·043	0·044	0·046	0·045
C04	0·000	0·000	0·000	0·000	0·156	0·167	0·183	0·193	0·045	0·047	0·050	0·050
C05	0·001	0·001	0·000	0·000	0·196	0·195	0·198	0·201	0·062	0·062	0·069	0·069
Average									**0·046**	**0·047**	0·051	0·050

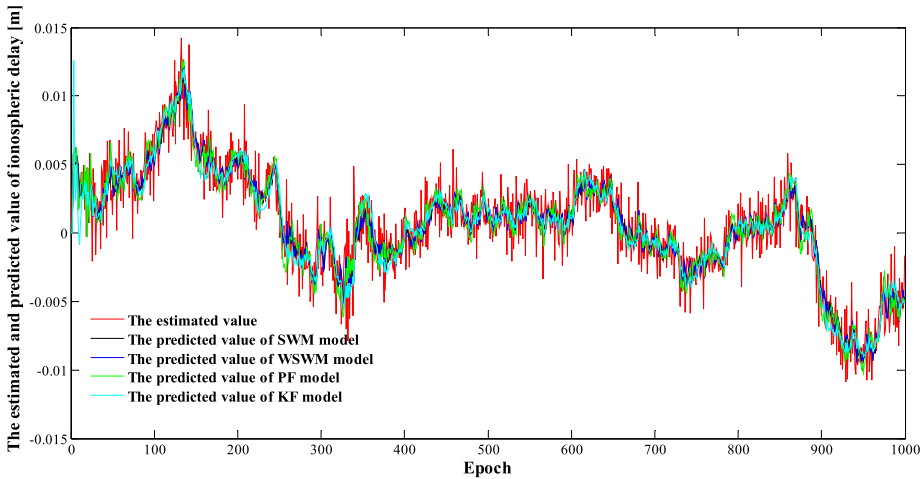Note: Bold font indicates preferred results.

Figure 3.   Estimated ionospheric delay and predicted values of the four models for satellite C01.

deviation) of ΔN_3 for each of the GEO satellites is presented in Table 2. It is evident that the STD is mostly <0·06 cycles, with an average value of 0·046 cycles, for which the corresponding rounding success rate is close to 100%. In addition, the prediction accuracies of the SWM and WSWM methods are slightly higher than the PF and KF methods. The main reason is that the ionospheric delay of GEO satellites is more stable over reasonably short periods, despite a certain degree of volatility. Therefore, we did not segment the accuracy statistics for GEO satellites.

The predictions of ionospheric delay for the GEO satellites derived from the four prediction models are shown in Figure 3. It can be seen that all four models produce a reasonable smoothing effect and that they are effective in overcoming the noise of the estimated ionospheric delay.

The differences between the predicted ionospheric values and the estimated values from the four improved prediction models for the C01 satellite are shown in Figure 4. It is apparent that the differences remain generally unchanged (that is, mostly within a range of 5 mm), which could both ensure high accuracy of the GF combination after ionospheric delay correction and ensure the accuracy of the repaired cycle slip.
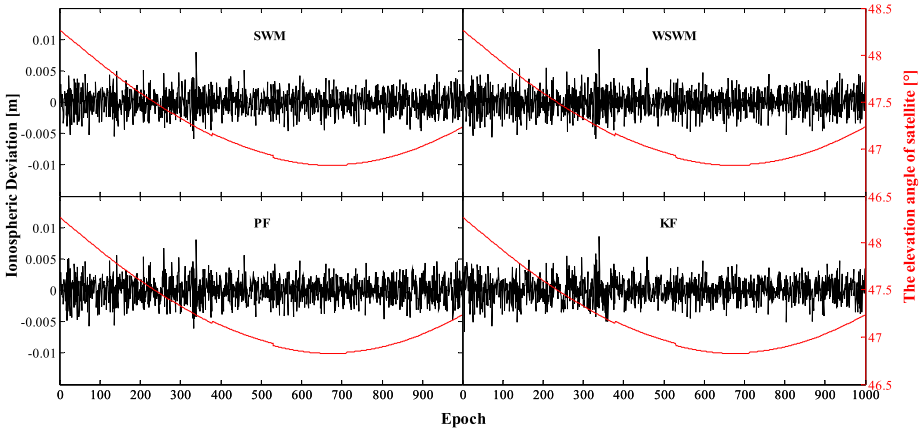
Figure 4. Difference between the estimated ionospheric delay and predicted values of the four prediction models for the C01 satellite: (top left) SWM, (top right) WSWM, (bottom left) PF, and (bottom right) KF.

Table 3. Rounding accuracy of ΔN_3 for IGSO and MEO satellites for elevation angles $>30°$(unit: cycles).

PRN	Mean				Maximum				STD			
	SWM	WSWM	PF	KF	SWM	WSWM	PF	KF	SWM	WSWM	PF	KF
C06	0·000	0·000	0·000	−0·001	0·230	0·230	0·179	0·175	0·044	0·044	0·044	0·046
C08	−0·001	−0·001	0·000	0·000	0·232	0·233	0·215	0·212	0·062	0·065	0·062	0·061
C09	0·000	0·000	−0·001	0·000	0·185	0·183	0·204	0·174	0·049	0·049	0·056	0·057
C11	−0·003	−0·003	0·002	0·001	0·200	0·189	0·221	0·207	0·070	0·072	0·073	0·074
C14	−0·002	−0·001	0·000	0·000	0·192	0·189	0·204	0·198	0·046	0·046	0·056	0·053
Average									**0·054**	**0·055**	0·058	0·058

Note: Bold font indicates preferred results.

Table 4. Rounding accuracy of ΔN_3 for IGSO and MEO satellites for elevation angles $<30°$ (unit: cycles).

PRN	Mean				Maximum				STD			
	SWM	WSWM	PF	KF	SWM	WSWM	PF	KF	SWM	WSWM	PF	KF
C07	−0·009	−0·008	−0·002	0·002	0·202	0·192	0·218	0·229	**0·077**	0·078	0·080	**0·077**
C08	−0·003	−0·002	−0·006	−0·008	0·180	0·210	0·184	0·177	**0·068**	0·073	0·070	0·070
C09	−0·002	−0·002	0·007	0·002	0·216	0·211	0·248	0·297	0·078	**0·077**	0·088	0·092
C10	−0·003	−0·003	0·001	0·007	0·378	0·360	0·349	0·361	0·087	0·089	0·089	**0·085**
C11	−0·027	−0·023	−0·007	−0·005	0·166	0·157	0·196	0·181	0·087	0·087	**0·084**	0·085
C14	−0·002	−0·002	−0·001	−0·001	0·235	0·232	0·223	0·227	0·078	**0·077**	0·083	0·082
Average									**0·079**	0·080	0·082	0·082

Note: Bold font indicates preferred results.

3.4. *Comparison of prediction model accuracy for IGSO and MEO satellites.* As described in Section 3.1, we segmented the data for IGSO and MEO satellites and set the satellite elevation angle threshold to 30°. Tables 3 and 4 present the rounding accuracy of ΔN_3 of the four prediction models for satellite elevation angles $>30°$ and $<30°$, respectively.

For satellite elevation angles $>30°$, the statistical accuracies of IGSO and MEO satellites are consistent with GEO satellites, and the SWM and WSWM methods are slightly better
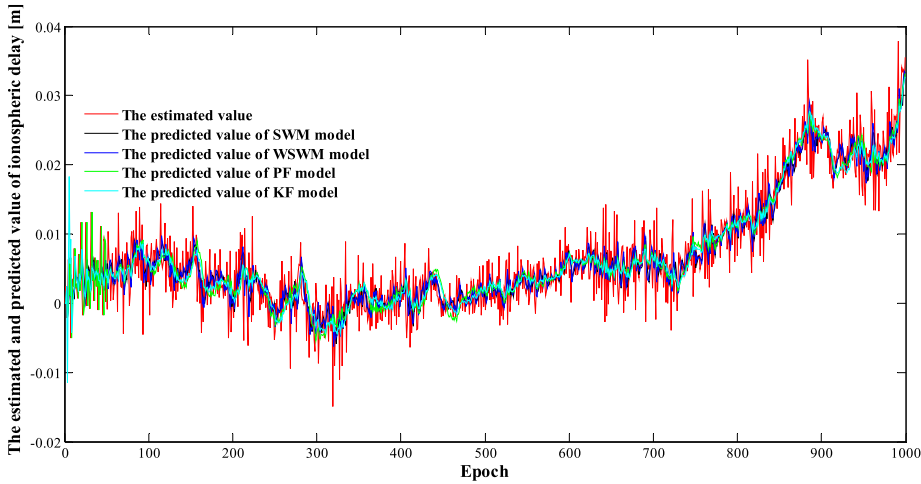
Figure 5.   Estimated ionospheric delay and predicted values of the four prediction models for satellite C08.

than the PF and KF methods (Table 3). This is mainly because ionospheric delay variation is small when the elevation angles of IGSO and MEO satellites are $>30°$. Therefore, using windowing and simple averaging is most stable and reliable. Moreover, the STD of the ΔN_3 rounding error is always $<0·07$ cycles. Considering that the rounding success rate of the EWL_1 and EWL_2 combinations is $>99·999997\%$, the results obtained using the prediction models in this paper suggest the final rounding success rate of BDS triple-frequency cycle slips is close to 100%.

Conversely, for satellite elevation angles $<30°$, the SWM model performs slightly better in comparison with the other models (Table 4). Even though the accuracy of *ION* prediction declines slightly, the STD of ΔN_3 rounding errors is $<0·1$ cycles (Teunissen and de Bakker, 2013), which ensures the rounding success rate of BDS triple-frequency observations is close to 100%.

Figures 5 and 6 show the ionospheric delay variation for the C08 and C11 satellites, respectively, based on the four improved prediction models. It can be seen that the maximum ionospheric delay variations of the C08 and C11 satellites reach 40 and 120 mm, respectively. Moreover, if ionospheric delay correction is not performed, the estimation of cycle slip will be incorrect, which will result in failure of the cycle–slip repair.

Figures 7 and 8 display the differences between the estimated ionospheric delay and the predicted values of the four prediction models for the C08 and C11 satellites, respectively. It is evident that as satellite elevation changes, the difference fluctuates considerably, especially when the satellite elevation angle is $<30°$. However, most of the ionospheric delay variation is within a range of 10 mm, which can ensure the rounding success rate of cycle–slip estimation is close to 100%. In addition, there is little difference between the four improved prediction models.

3.5. *The results of cycle slip detection and repair.*   To illustrate the efficiency of cycle–slip detection and repair, Figures 9(a)-(c) show the rounding errors of the estimates of EWL_1, EWL_2, and ΔN_3 for the C01, C08 and C11 satellites, respectively. The rounding errors of ΔN_3 for the C08 and C11 satellites are shown in Figures 9(b) and 9(c), respectively, based on the improved prediction models (the SWM, as an example, ignores the
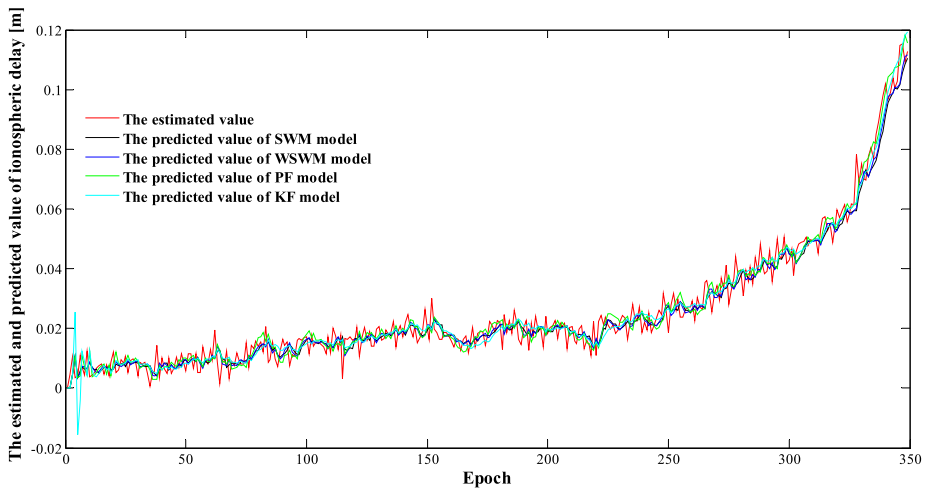
Figure 6.   Estimated ionospheric delay and predicted values of the four prediction models for satellite C11.
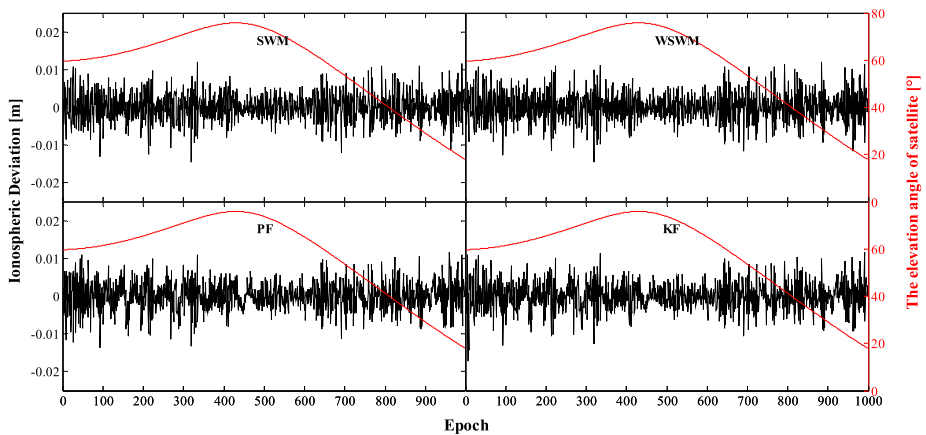

Figure 7.   Difference between the estimated ionospheric delay and predicted values of the four prediction models for the C08 satellite: (top left) SWM, (top right) WSWM, (bottom left) PF, and (bottom right) KF.

differences among the different models). It can be seen that the maximum rounding error of ΔN_3 for the C08 and C11 satellites is 0·6 and 2·0 cycles (or 40 and 120 mm), respectively. If the residual ionospheric delay corrections were not performed, the estimation of cycle slip would be incorrect, resulting in failure of the cycle–slip repair. Compared with Chang et al. (2018), the use of the ionospheric prediction models in this paper ensures the rounding accuracy of ΔN_3 is equivalent to that of EWL_1 and EWL_2. Thus, it is shown to be effective in improving the overall accuracy of cycle–slip repair.

In addition, no case was found in Figures 9(a)-(c) where the cycle–slip detection amount was >0·5 cycles, after correcting the residual ionospheric delay, which means the cycle–slip repair was all correct in this data processing.

3.6.   *Cycle slip detection and repair under high ionospheric activity.*   To verify the effectiveness of the four models in repairing cycle slip under conditions of high ionospheric
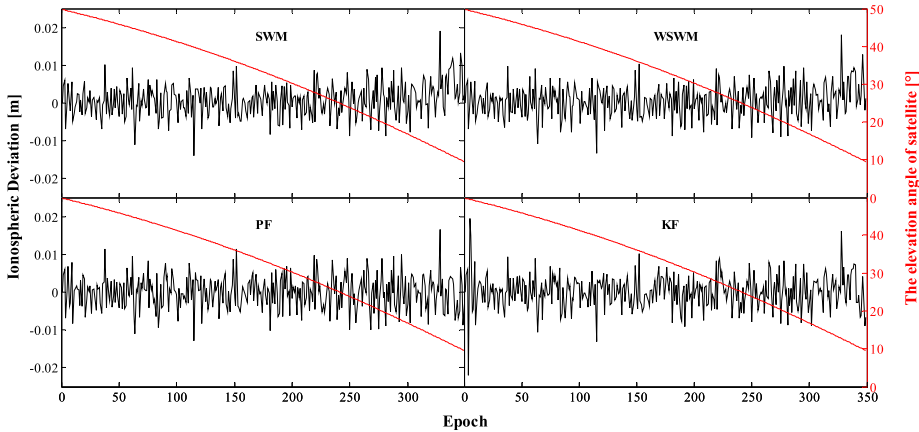
Figure 8. Difference between the estimated ionospheric delay and predicted values of the four prediction models for the C11 satellite: (top left) SWM, (top right) WSWM, (bottom left) PF, and (bottom right) KF.

activity, data from station SHA1 obtained on 26 August 2018 was used for analysis. The sampling interval was 30 s and the period of observation was 23 h (data for the final hour was missing). The ionospheric delay on this day was active and the corresponding Kp index reached a value of seven. The corresponding ionospheric delay variation is shown in Figure 10. Compared with the values obtained during the stable ionosphere period (Figures 3, 5 and 6), Figure 10 shows the ionospheric delay variation of station SHA1 on 26 August 2018 was more active, with the value for many satellites reaching 2–4 cm.

The rounding errors of EWL combination float estimations are shown in Table 5. Compared with Table 1 (ionosphere not active), the STD is no larger and all values are <0.09 cycles, except for the C05 satellite (corresponding satellite elevation angles range from $14°–16°$); however, the maximum of EWL_2 has a large increase. This is primarily due to the active ionospheric variance and shorter wavelength of EWL_2. However, as can be seen from the maximum values, the rounding values of EWL combinations were acceptable for all satellites and all epochs.

The rounding accuracy of ΔN_3 for all GEO satellites is presented in Table 6. On the one hand, it is evident that the STD has been greatly increased (up to 0.064 cycles) in comparison with that derived under conditions with a stable ionosphere. Moreover, the C05 satellite has an epoch cycle–slip repair error due to the lower satellite elevation angle ($15°$), and the maximum deviation of ΔN_3 was >0.5 cycles. On the other hand, the experimental results show the accuracies of the SWM and KF methods were higher, while the performance of the PF method was worse.

We segmented the data for IGSO and MEO satellites and set the satellite elevation angle threshold to $30°$. Tables 7 and 8 present the statistical accuracies of the four prediction models for satellite elevation angles $>30°$ and $<30°$, respectively. For satellite elevation angles $>30°$, the STD of the ΔN_3 rounding error had a small increase (up to 0.58 cycles). However, there was no incorrect rounding of ΔN_3 for any of the satellites in all epochs. In addition, the experimental results show the accuracies of the SWM and KF methods were higher, while the performance of the PF method was worse.
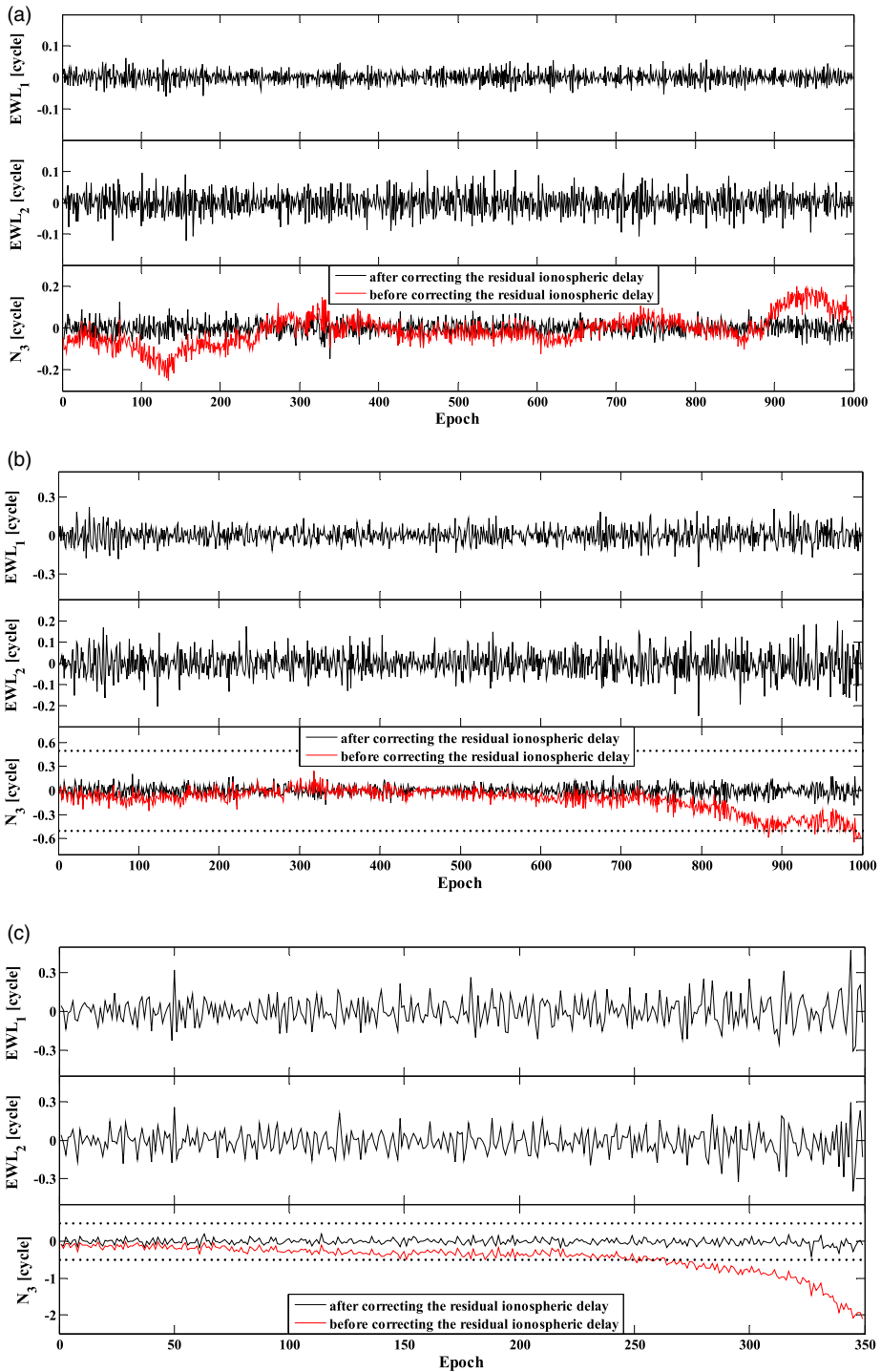
Figure 9.   Test values of cycle–slip detection. (a) Satellite C01. (b) Satellite C08. (c) Satellite C11.
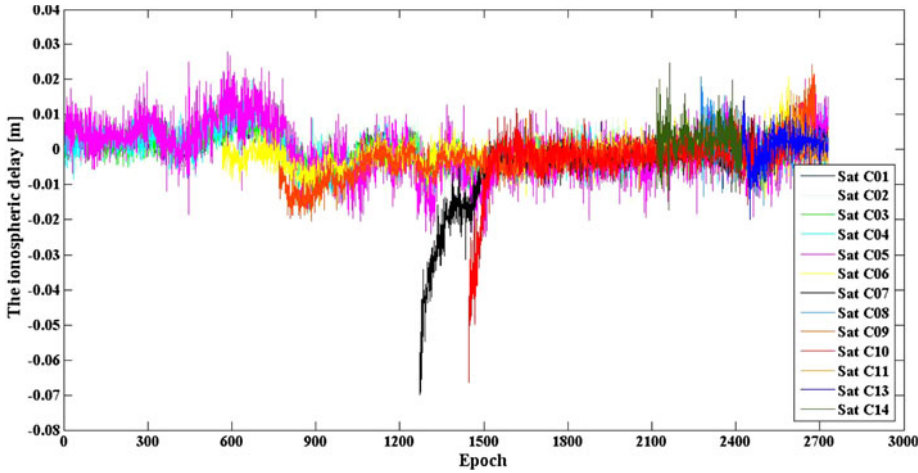
Figure 10.   The ionospheric delay variation of station SHA1 on 26 August 2018.

Table 5.   Rounding error of EWL combination under high ionospheric activity (unit: cycles).

PRN	Mean		Maximum		STD	
	EWL_1	EWL_2	EWL_1	EWL_2	EWL_1	EWL_2
C01	0·000	0·000	0·043	0·194	0·010	0·044
C02	0·000	0·000	0·070	0·327	0·018	0·086
C03	0·000	0·000	0·048	0·220	0·013	0·057
C04	0·000	0·000	0·051	0·191	0·013	0·048
C05	0·000	0·000	0·099	0·379	0·025	0·102
Average					0·016	0·067
C06	0·000	0·002	0·111	0·486	0·017	0·062
C07	0·000	−0·002	0·092	0·319	0·018	0·064
C08	0·000	0·000	0·138	0·359	0·018	0·065
C09	0·000	0·002	0·122	0·399	0·019	0·065
C10	0·000	−0·002	0·098	0·467	0·019	0·072
Average					0·018	0·066
C11	0·001	−0·003	0·124	0·322	0·034	0·089
C13	0·000	0·000	0·110	0·411	0·020	0·067
C14	0·000	−0·001	0·144	0·306	0·035	0·082
Average					0·029	0·079

Table 6.   Rounding accuracy of ΔN_3 for GEO satellites under high ionospheric activity (unit: cycles).

PRN	Mean				Maximum				STD			
	SWM	WSWM	PF	KF	SWM	WSWM	PF	KF	SWM	WSWM	PF	KF
C01	0·000	0·000	0·000	0·000	0·156	0·155	0·181	0·171	0·046	0·048	0·050	0·045
C02	0·000	0·000	0·000	0·000	0·219	0·224	0·249	0·197	0·054	0·057	0·060	0·053
C03	0·000	0·000	0·000	0·000	0·210	0·217	0·250	0·207	0·055	0·058	0·061	0·054
C04	0·000	0·000	0·000	0·000	0·242	0·253	0·257	0·235	0·060	0·063	0·066	0·059
C05	0·000	0·000	0·000	0·000	*0·541*	*0·588*	*0·594*	*0·533*	0·106	0·112	0·116	0·104
Average									**0·064**	0·067	0·070	**0·063**

Note: Bold font indicates preferred results; italic font indicates failure of cycle–slip repair.

Table 7. Rounding accuracy of ΔN_3 for IGSO and MEO satellites for elevation angles $>30°$ under high ionospheric activity (unit: cycles).

PRN	Mean				Maximum				STD			
	SWM	WSWM	PF	KF	SWM	WSWM	PF	KF	SWM	WSWM	PF	KF
C06	0·000	0·000	0·000	0·000	0·206	0·201	0·220	0·187	0·051	0·054	0·056	0·050
C07	0·000	0·000	0·000	0·000	0·252	0·266	0·281	0·270	0·054	0·056	0·059	0·052
C08	0·000	0·000	0·000	0·000	0·286	0·289	0·348	0·253	0·062	0·065	0·069	0·060
C09	0·000	0·000	0·000	0·000	0·170	0·166	0·181	0·181	0·054	0·056	0·059	0·053
C10	−0·001	−0·001	0·000	0·000	0·378	0·348	0·411	0·380	0·063	0·065	0·070	0·061
Average									**0·057**	0·059	0·063	**0·055**
C11	−0·001	0·000	0·001	0·000	0·173	0·183	0·222	0·182	0·061	0·064	0·067	0·062
C13	0·000	0·000	0·000	0·000	0·172	0·180	0·205	0·175	0·051	0·052	0·055	0·049
C14	−0·002	−0·001	0·000	0·002	0·272	0·310	0·336	0·270	0·072	0·074	0·077	0·070
Average									**0·059**	0·061	0·064	**0·057**

Note: Bold font indicates preferred results.

Table 8. Rounding accuracy of ΔN_3 for IGSO and MEO satellites for elevation angles $<30°$ under high ionospheric activity (unit: cycles).

PRN	Mean				Maximum				STD			
	SWM	WSWM	PF	KF	SWM	WSWM	PF	KF	SWM	WSWM	PF	KF
C06	−0·002	−0·002	0·002	0·002	0·409	0·428	0·365	*0·558*	0·105	0·110	0·117	0·118
C07	−0·017	−0·014	0·000	−0·002	0·352	0·367	0·385	0·324	0·094	0·097	0·101	0·110
C08	0·001	0·001	−0·001	−0·001	0·309	0·343	0·343	0·327	0·106	0·112	0·117	0·103
C09	−0·004	−0·004	0·000	−0·002	0·359	0·360	0·320	0·453	0·097	0·100	0·101	0·106
C10	−0·011	−0·009	0·000	−0·001	0·379	0·409	0·433	0·403	0·111	0·117	0·117	0·121
Average									**0·103**	0·107	0·111	0·112
C11	0·000	0·000	0·000	0·001	0·474	0·470	*0·501*	0·434	0·102	0·103	0·107	0·097
C13	0·000	0·000	0·000	−0·001	0·358	0·399	0·430	0·356	0·107	0·111	0·113	0·105
C14	−0·002	−0·004	−0·003	−0·001	*0·533*	*0·614*	*0·660*	0·466	0·112	0·119	0·114	0·104
Average									0·107	0·111	0·111	**0·102**

Note: Bold font indicates preferred results; italic font indicates failure of cycle–slip repair.

Table 9. Results of cycle-slip repair under high ionospheric activity.

PRN	Total number of epochs	No. incorrect repair without correcting ionosphere	No. incorrect repair with correcting ionosphere			
			SWM	WSWM	PF	KF
C01	2734	0	0	0	0	0
C02	2734	0	0	0	0	0
C03	2734	0	0	0	0	0
C04	2734	0	0	0	0	0
C05	2731	2	1	2	2	1
C06	2227	9	0	0	0	1
C07	2139	204	0	0	0	0
C08	2053	0	0	0	0	0
C09	2138	45	0	0	0	0
C10	2044	171	0	0	0	0
C11	484	7	0	0	1	0
C13	2012	0	0	0	0	0
C14	803	0	1	1	3	0

For satellite elevation angles <30°, it is evident from the maximum values that cycle–slip repair failed for several satellites (for example, C06, C11 and C14), mainly because of the large ionospheric variation. In addition, the experimental results show the SWM and KF methods were superior for IGSO and MEO satellites, respectively.

To clarify the effect of adding the correction value for ionospheric delay and the effect of cycle–slip repair using the four models, Table 9 shows the statistics of cycle–slip detection and repair for all satellite observations. The results show the ionospheric delay correction can greatly improve the success rate of cycle–slip repair (that is, an improvement from 98·411% to 99·993%). Moreover, it is found that failure of cycle–slip repair occurs continually when the satellite elevation angle is <30°. This is considered attributable mainly to large variation of the ionospheric delay, which means it is necessary to correct the residual ionospheric delay.

4. CONCLUSIONS.   Based on the influence of ionospheric delay variation on the observation accuracy of the GF phase combination, four classical representative prediction models were used to detect and repair the cycle slip of two sets of measured BDS data that separately reflected stable and active ionospheric conditions. The principal objective of this study was to evaluate the efficacy of a three-step method proposed to detect and repair cycle slip using two EWL code–phase and one GF phase combination observations. The experimental results revealed the following findings:

(1) The STD of rounding accuracy of the EWL code–phase combination observations was <0·10 cycles, with a corresponding success rate of close to 100%. GEO satellites had the highest accuracy, followed by IGSO and then MEO satellites. It was established that there is no requirement to correct the residual ionospheric delay for the EWL combination, even under conditions of high ionospheric activity.

(2) For IGSO and MEO satellites with satellite elevation angles >30°, or GEO satellites under any conditions, the ionospheric delay variation is small, and the efficiency and success rate of cycle–slip repair using the four models showed little difference, although the SWM methods were slightly better.

(3) For IGSO and MEO satellites with satellite elevation angles <30°, even under highly active ionospheric activity, to ensure the success rate of rounding estimators, the residual ionosphere must be predicted to correct NL combination observations. Of the four models considered, the SWM and KF methods were found to be superior.

(4) Using the proposed three-step method to detect and repair cycle slip for BDS triple-frequency observation data, the success rate of cycle–slip repair was found to be close to 100%, even under conditions of high ionospheric activity.

The advantage of this model is that it can detect and repair the cycle slip of data with a high success rate and simple processing. Even for data with a 30 s sampling interval under conditions of high ionospheric activity, the success rate of cycle–slip repair was found to be close to 100%. This study did not consider the correlation between epochs and parameters, nor did it consider the non-integer case of cycle slip; both these subjects should be investigated in future study.

REFERENCES

Blewitt, G. (1990). An Automatic Editing Algorithm for GPS data. *Geophysical Research Letters*, **17**, 199–202.

Cai, C., Liu, Z., Xia, P. and Dai, W. (2012). Cycle slip detection and repair for undifferenced GPS observations under high ionospheric activity. *GPS Solutions*, **17**, 247–260.

Chang, G., Xu, T., Yao, Y. and Wang, Q. (2018). Adaptive Kalman filter based on variance component estimation for the prediction of ionospheric delay in aiding the cycle slip repair of GNSS triple-frequency signals. *Journal of Geodesy*, **92**, 1241–1253.

Cocard, M., Bourgon, S., Kamali, O. and Collins, P. (2008). A systematic investigation of optimal carrier-phase combinations for modernized triple-frequency GPS. *Journal of Geodesy*, **82**, 555–564.

Gerdan, G. P. (1995). A comparison of four methods of weighting double difference pseudorange measurements. *Australian Surveyor*, **40**, 60–66.

Hatch, R. R. (1982). The synergism of GPS code and carrier measurements. *International Geodetic Symposium on Satellite Doppler Positioning*, 1213–1231.

Huang, L., Lu, Z., Zhai, G., Ouyang, Y., Huang, M., Lu, X., Wu, T. and Li, K. (2015). A new triple-frequency cycle slip detecting algorithm validated with BDS data. *GPS Solutions*, **20**, 761–769.

Li, B. F., Verhagen, S. and Teunissen, P. J. G. (2014). Robustness of GNSS integer ambiguity resolution in the presence of atmospheric biases. *GPS Solutions*, **18**, 283–296.

Li, J., Yang, J. and Xu, J. (2011). Real-time cycle-slip detection and repair based on code-phase combinations for GNSS triple-frequency undifferenced observations. *Acta Geodaetica et Cartographica Sinica*, **40**, 717–722.

Li, Z., Gao, J. and Wang, J. (2016). Inertial Aided Cycle Slip Detection and Repair for PPP/INS Tightly Coupled Navigation. *The Journal of Navigation*, **69**, 1357–1378.

Liu, Z. (2010). A new automated cycle slip detection and repair method for a single dual-frequency GPS receiver. *Journal of Geodesy*, **85**, 171–183.

Melbourne, W. (1985). The case for ranging in GPS-based geodetic systems. *Proceedings of the First International Symposium on precise positioning with GPS*. 373–386.

Richert, T. and El-Sheimy, N. (2007). Optimal linear combinations of triple frequency carrier phase data from future global navigation satellite systems. *GPS Solutions*, **11**, 11–19.

Teunissen, P. J. G. (1995). The least-squares ambiguity decorrelation adjustment: A method for fast GPS integer ambiguity estimation. *Journal of Geodesy*, **70**, 65–82.

Teunissen, P. J. G. (2002). The parameter distributions of the integer GPS model. *Journal of Geodesy*, **76**, 41–48.

Teunissen, P. J. G. and de Bakker, P. F. (2013). Single-receiver single-channel multi-frequency GNSS integrity: outliers, slips, and ionospheric disturbances. *Journal of Geodesy*, **87**, 161–177.

Urquhart, L. (2009). *An analysis of multi-frequency carrier phase linear combinations for GNSS*. Senior technical report, Department of Geodesy and Geomatics Engineering Technical Report No. 263, University of New Brunswick, Fredericton, New Brunswick, Canada. http://www2.unb.ca/gge/Pubs/TR263.pdf

Wübbena, G. (1985). Software developments for geodetic positioning with GPS using TI-4100 code and carrier measurements. *Proceedings of the First International Symposium on precise positioning with the Global Positioning System*. US Department of Commerce, 403–412.

Yao, Y. F., Gao, J. X., Wang, J., Hu, H. and Li, Z. K. (2016). Real-time cycle-slip detection and repair for BeiDou triple-frequency undifferenced observations. *Survey Review*, **48**, 367–375.

Zhang, X. and Li, P. (2015). Benefits of the third frequency signal on cycle slip correction. *GPS Solutions*, **20**, 451–460.

Zhao, Q., Sun, B., Dai, Z., Hu, Z., Shi, C. and Liu, J. (2014). Real-time detection and repair of cycle slips in triple-frequency GNSS measurements. *GPS Solutions*, **19**, 381–391.